Commun. Comput. Phys.
doi: 10.4208/cicp.2019.js60.07

Vol. **26**, No. 5, pp. 1444-1470
November 2019

An Efficient and Unconditionally Energy Stable Scheme for Simulating Solid-State Dewetting of Thin Films with Isotropic Surface Energy†

Qiong-Ao Huang[1], Wei Jiang[1,2] and Jerry Zhijian Yang[1,2,*]

[1] *School of Mathematics and Statistics, Wuhan University, Wuhan, 430072, China.*
[2] *Hubei Key Laboratory of Computational Sciences, Wuhan University, Wuhan, 430072, China.*

Received 28 February 2019; Accepted (in revised version) 7 May 2019

Abstract. In this paper, we propose highly efficient, unconditionally energy-stable numerical schemes to approximate the isotropic phase field model of solid-state dewetting problems by using the invariant energy quadratization (IEQ) method. The phase field model is governed by the isotropic Cahn-Hilliard equation with degenerate mobilities and dynamic contact line boundary conditions. By using the backward differential formula to discretize temporal derivatives, we construct linearly first- and second-order IEQ schemes for solving the model. It can be rigorously proved that these numerical schemes are unconditionally energy-stable and satisfy the total mass conservation during the evolution. By performing numerical simulations, we demonstrate that these IEQ-based schemes (including the first-order IEQ/BDF1, second-order IEQ/BDF2) are highly efficient, accurate and energy-stable. Furthermore, many interesting dewetting phenomena (such as the hole dynamics, pinch-off), are investigated by using the proposed IEQ schemes.

AMS subject classifications: 74K35, 65M06, 65M12, 35K55

Key words: Solid-state dewetting, surface diffusion, phase-field model, degenerate Cahn-Hilliard equation, invariant energy quadratization, unconditionally energy-stable.

1 Introduction

Solid-state dewetting of thin films on substrates is a ubiquitous phenomenon in thin film technologies and materials science, which has been observed in a wide range of systems

†Dedicated to Professor Jie Shen on the occasion of his 60th birthday.
*Corresponding author. *Email addresses:* jiangwei1007@whu.edu.cn (W. Jiang), zjyang.math@whu.edu.cn (J. Z. Yang)

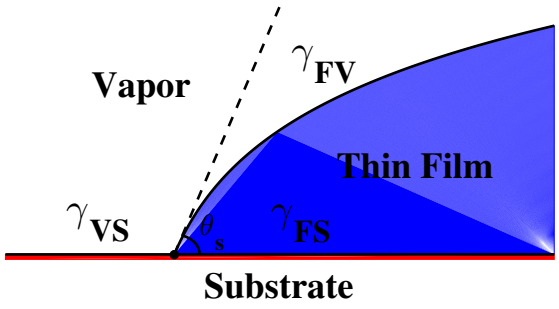

Figure 1: A schematic illustration of the three interfaces which meet with each other at the contact point/line in solid-state dewetting, where θ_s is Young's contact angle.

and is of considerable technological interest [1–6] (e.g., see the recent review papers by C. V. Thompson [7] and F. Leroy *et. al.* [8]). Nowadays, the solid-state dewetting has been widely used in thin film solar cells [9], optical and magnetic devices [10], sensor devices [11], catalyzing the growth of carbon nanotubes [12], semiconductor nanowires [13], etc. Especially, in recent years, the solid-state dewetting has attracted increasing attention both because of interest in the underlying pattern formation physics and its potential technology applications [14–19].

The dewetting of thin solid films deposited on substrates is very similar to the dewetting phenomena of liquid films on substrates, which has been investigated in numerous theoretical and experimental studies [20–24] and recently reviewed in [25]. For example, for both the phenomena, dewetting and pinch-off may happen when an initially continuous and long thin film is bonded to a rigid substrate and eventually an array of isolated particles will form. However, they have many important major differences. For example, their mass transport processes are totally different, while the solid-state dewetting is usually dominated by surface diffusion rather than fluid dynamics. The solid-state dewetting can be modeled as a type of interface-tracking problem for the evolution via surface diffusion flow, coupled with contact line migration [16, 26–30]. More specifically, the contact line is a triple line (where the film, substrate, and vapor phases meet, shown in Fig. 1) that migrates as the curve/surface evolves.

In general, the dewetting problem belongs to a more general class of capillarity-controlled interface/surface evolution problems. The solid-state dewetting problem is mainly studied by using two different mathematical models, i.e., sharp-interface model and phase-field model. Behind these models, surface diffusion flow and contact line migration have been recognized as the two main kinetic processes during the solid-state dewetting evolution. The first sharp-interface model for solid-state dewetting was proposed by Srolovitz and Safran [31] to investigate the hole growth during the dewetting under the assumption of isotropic surface energy, small slope profile and cylindrical symmetry. Subsequently, the sharp-interface model was numerically solved without the small-slope assumption by using "marker particle method" (i.e., finite differ-

ence schemes) in two dimensions (2D) [14] and three dimensions (3D) [32]. Recently, sharp-interface models were obtained rigorously via the energy variational method for the temporal evolution of open curves in 2D for the solid-state dewetting of thin films with weakly and strongly anisotropic surface energies, and these models were further extended to the axisymmetric geometry case [33] and fully 3D case [34]. For details, we refer to [17, 26–30] and references therein. However, for solid-state dewetting problems, one of the main difficulty for these interface-capturing methods lies in how to deal with the complex boundary conditions which result from contact line migrations. Recently, a phase field model by using the Cahn-Hilliard equation with degenerate mobilities and nonlinear boundary conditions along the substrate has been proposed for simulating the solid-state dewetting with isotropic surface energy [16], and this method was recently extended to the weakly anisotropic surface energy case [35]. One of the major advantages of the phase field approach over other explicit interface tracking approaches is its ability to naturally capture the types of topological events that are observed in experiments. It is also straightforward to generalize a simulation from lower to higher spatial dimensions using this approach.

On the other hand, the moving contact line problem that exists in many physical processes when the mixture interface (e.g. film-vapor interface in this paper) touches a solid wall (or substrate), for instance, dewetting, spray cooling of surfaces, spray coating, etc. For such cases, the simple no-slip boundary conditions imply that the position of the contact line does not move; therefore, a non-physical velocity discontinuity will occur at the moving contact line [36]. This problem has always been an appealing and challenging topic for mathematical modeling and simulations. To tackle this problem, Qian *et al.* [37, 38] proposed the so called dynamical contact line boundary condition in fluid mechanics, and they use explicit schemes to obtain the numerical solutions, but they often require a very small time step to ensure the numerical stability. Recently, several attempts have been made to alleviate the numerical stability restriction on the time step, such as the works by Wang *et al.* [39–41], Salgado [42], Aland and Chen [43], Shen and Yang [44–46]. However, these numerical schemes are either nonlinearly coupled which often require some efficient iterative solvers and need relatively high computational cost, or linearly decoupled but which can not to be proved to be unconditionally energy-stable from mathematics. Therefore, it is a still challenging problem about how to design an unconditionally energy stable time-stepping numerical schemes.

In the literature, there exist a lot of famous numerical approaches which have been proposed for dealing with phase-field models (i.e., Allen-Cahn and Cahn-Hilliard equations), such as the semi-implicit spectral method (e.g., [47–49]), the convex splitting method (e.g., [50–52]) and the stabilization method (e.g., [16, 53, 54]). Very recently, motivated by the Lagrange multiplier approach [55], Yang *et al.* proposed the so called invariant energy quadratization (IEQ) approach for solving a large class of gradient flow models [56–62]. This approach can lead to unconditionally energy stable, linear, high-order schemes. The essential idea of the approach is first to transform the free energy density function into a quadratic function of a set of new variables; then, for the refor-

mulated model in terms of these new variables, they can prove the energy dissipation property. Although the IEQ approach has proven to be a very powerful tool to constructing energy stable schemes, it requires that the free energy density function is bounded below, which may not hold for some physically interesting models. Furthermore, Shen *et. al.* introduced the so called scalar auxiliary variable (SAV) approach [63–66], which is built upon the IEQ approach but the key difference is to transform the free energy (not the free energy density function) into a quadratic function of a set of new variables, and this approach requires that the free energy function (instead of free energy density function) is bounded below. This SAV approach inherits some advantages of IEQ approach, e.g., it only requires to solve linear equations with constant coefficients at each time step. For the Cahn-Hilliard equation with a constant mobility, SAV scheme only requires to solve linear equations with constant coefficients at each time step, while IEQ needs to solve variable coefficient linear equations at each time step. However, for the Cahn-Hilliard equation with a variable mobility, SAV scheme needs to solve a nonlocal variable coefficient linear equations at each time step [67], while IEQ still only needs to solve local variable coefficient linear equations [68]. Therefore, by considering the computational cost and storage needs, we adopt the IEQ-based scheme in this paper for solving solid-state dewetting problems. Based on the IEQ approach, we aim at developing some efficient, unconditionally energy stable schemes for solving the isotropic phase field model of solid-state dewetting problems, in order to investigate complicated solid-state dewetting phenomena.

The rest of the paper is organized as follows. In Section 2, we briefly present an isotropic phase field model with dynamic contact line boundary conditions for simulating solid-state dewetting problems. In Section 3, we construct a first-order and a second-order, unconditionally energy-stable time-stepping numerical schemes for solving the phase field model, and rigorously from mathematics prove that the resulted linear system admits a unique solution, and that these solutions of the schemes also satisfy the energy dissipation and mass conservation properties. In Section 4, we present ample numerical simulations to demonstrate the accuracy and efficiency of the proposed schemes, and many interesting dewetting phenomena (including the hole dynamics, pinch-off) are also investigated by using the proposed numerical schemes. Finally, we draw some conclusions in Section 5.

2 Phase field model

In this section, we first give a brief introduction to the phase field model for simulating solid-state dewetting of thin films on a rigid solid substrate, and this phase field model was previously proposed in 2012 by Jiang *et al.* [16]. The basic idea behind the phase field method is to describe the interface evolution by a partial differential equation (PDE) for the evolution of an auxiliary field (the phase field) that plays the role of an order parameter. This phase field takes two distinct values (e.g. $+1$ and -1) in each of the two phases

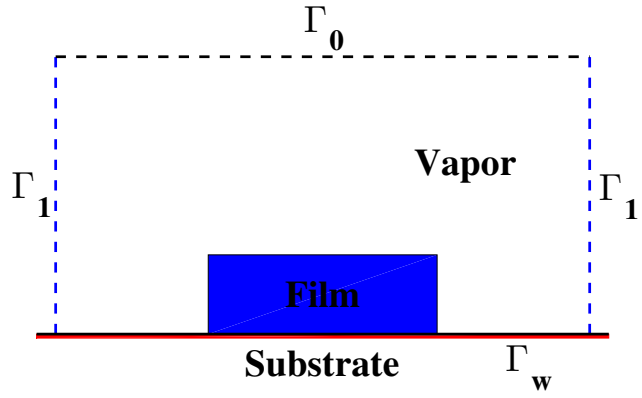

Figure 2: A schematic illustration of the set-up of the phase field approach.

bounding an interface and varies smoothly across the interface, i.e. interfaces are diffuse in phase field simulations. In the phase field model, the interface is considered as a transition layer (ε is usually used to represent the width of the layer) over which a continuous, but steep change of some physical quantities occurs. The phase field model can be naturally derived from the energy-based variational approach, therefore, the developed governing system is normally well-posed and satisfies a thermodynamically consistent energy dissipation law. Moreover, the presence of the energy law serves as a guide line for the design of energy stable numerical schemes, and further to perform reliable numerical simulations.

Without loss of generality, we put the simulated system into a bounded rectangular box, labeled as Ω with boundary $\partial\Omega=\Gamma_0\cup\Gamma_1\cup\Gamma_w$ which has an outward-pointing unit normal $\mathbf{n}$ (cf. Fig. 2). The reason why we choose the above computational domain is that it is easy to handle and adequate for the dewetting of a solid film on a substrate. The phase field function $\phi=\phi(\mathbf{x})$ is introduced such that the zero-level set $\{\mathbf{x}|\phi(\mathbf{x})=0\}$ represents the film/vapor interface, while $\{\mathbf{x}|\phi(\mathbf{x})>0\}$ represents the film phase and $\{\mathbf{x}|\phi(\mathbf{x})<0\}$ the vapor phase. If we assume that the film-vapor interface energy is isotropic, then the total free energy of the system can be written in the following phase-field framework [16],

$$W[\phi]=W_{FV}+W_w=\int_\Omega f_{FV}(\phi)d\mathbf{x}+\int_{\Gamma_w} f_w(\phi)ds, \tag{2.1}$$

where W_{FV} represents the combined energy of the thin film and vapor phases, W_w represents the wall energy, and f_{FV} and f_w are the corresponding energy densities, respectively, which are defined as follows:

$$f_{FV}(\phi)=F(\phi)+\frac{\varepsilon^2}{2}|\nabla\phi|^2, \tag{2.2}$$

$$f_w(\phi)=\frac{\varepsilon\cos\theta_s}{3\sqrt{2}}(\phi^3-3\phi)+\frac{\sqrt{2}\varepsilon}{3}\frac{\gamma_{VS}+\gamma_{FS}}{\gamma_{FV}}, \tag{2.3}$$

where $F(\phi)=\frac{1}{4}(\phi^2-1)^2$ is the well-known Ginzburg-Landau double-well potential, ε is a small parameter related to the interface width, and $\theta_s\in[0,\pi]$ is the prescribed contact angle between the free interface and the solid substrate determined by the isotropic Young equation, i.e. $\cos\theta_s=(\gamma_{VS}-\gamma_{FS})/\gamma_{FV}$, where γ_{FV}, γ_{FS} and γ_{VS} are, respectively, the interface energy (density) describing the interfaces between film and vapor, film and substrate, and vapor and substrate (see Fig. 1). It should be noted that, we already multiply the total free energy W in (2.1) by the normalization factor ε/λ_m, where λ_m represents the mixing energy density and $\lambda_m=\frac{3\sqrt{2}}{4}\gamma_{FV}$ to ensure the Γ-convergence to the corresponding functional in the sharp-interface limit [16,69].

The following governing equations can be derived as a gradient flow of the energy functional (2.1) in H^{-1} space [16]:

$$\frac{\partial\phi}{\partial t}=\nabla\cdot(M(\phi)\nabla\mu),\qquad \text{in } \Omega, \tag{2.4}$$

$$\mu=\frac{\delta W}{\delta\phi}=\phi^3-\phi-\varepsilon^2\Delta\phi,\qquad \text{in } \Omega, \tag{2.5}$$

with the following dynamic boundary conditions:

$$\frac{\partial\phi}{\partial t}=-\eta\left[\varepsilon\frac{\partial\phi}{\partial\mathbf{n}}+\frac{\sqrt{2}}{2}(\phi^2-1)\cos\theta_s\right],\quad \frac{\partial\mu}{\partial\mathbf{n}}=0,\qquad \text{on } \Gamma_w, \tag{2.6}$$

$$\frac{\partial\phi}{\partial\mathbf{n}}=0,\quad \frac{\partial\mu}{\partial\mathbf{n}}=0,\qquad \text{on } \partial\Omega\backslash\Gamma_w, \tag{2.7}$$

where $M(\phi)\geq 0$ is a phase function-dependent diffusive mobility, and here the boundary condition can be viewed as the L^2-gradient flow for dissipating the total free energy with respect to the contact lines (see the similar ideas about the sharp-interface model for simulating solid-state dewetting [26] and triple junction migration [70]), and the constant $\eta(>0)$ represents the contact line mobility. In the literature, the mobility function is often chosen as a degenerate type, i.e., $M_0(\phi)=|1-\phi^2|^k$, $k=1,2,\cdots$, in order to make its sharp-interface limit as ε goes to zero as close as possible to the interface evolution via surface diffusion flow [16,71–73]. Such special choice for the mobility leads to a number of mathematical difficulties since it is degenerate (i.e., $\min(M_0(\phi))=0$), e.g., the well-posedness of the discrete schemes. In order to tackle these difficulties, in this paper we use a regularized mobility function as $M(\phi)=|1-\phi^2|^k+\varepsilon_M$ for $0<\varepsilon_M\ll 1$, where we choose $\varepsilon_M=10^{-8}$ in the numerical simulations.

We can easily show that the total free energy functional $W(t)$ defined in (2.1) is always dissipative during the evolution:

$$\begin{aligned}\frac{dW(t)}{dt}&=\int_\Omega\left(F'(\phi)\phi_t+\varepsilon^2\nabla\phi\cdot\nabla\phi_t\right)d\mathbf{x}+\int_{\Gamma_w}\frac{\varepsilon\cos\theta_s}{\sqrt{2}}(\phi^2-1)\phi_t ds\\&=\int_\Omega\mu\phi_t d\mathbf{x}+\int_{\partial\Omega}\varepsilon^2\frac{\partial\phi}{\partial\mathbf{n}}\phi_t ds+\int_{\Gamma_w}\frac{\varepsilon\cos\theta_s}{\sqrt{2}}(\phi^2-1)\phi_t ds\end{aligned}$$

$$
\begin{aligned}
&= \int_\Omega \mu \nabla\cdot(M(\phi)\nabla\mu)d\mathbf{x} + \int_{\Gamma_w}\left[\varepsilon^2\frac{\partial\phi}{\partial\mathbf{n}} + \frac{\varepsilon\cos\theta_s}{\sqrt{2}}(\phi^2-1)\right]\phi_t ds \\
&= -\int_\Omega M(\phi)|\nabla\mu|^2 d\mathbf{x} - \frac{\varepsilon}{\eta}\int_{\Gamma_w}(\phi_t)^2 ds \le 0,
\end{aligned} \tag{2.8}
$$

and the boundary conditions $(2.6)_2$ and $(2.7)_2$ implies that the total mass $m(t)$ is conservative:

$$
\frac{dm(t)}{dt} = \frac{d}{dt}\int_\Omega \phi d\mathbf{x} = \int_\Omega \phi_t d\mathbf{x} = \int_\Omega \nabla\cdot(M(\phi)\nabla\mu)d\mathbf{x} = \int_{\partial\Omega} M(\phi)\frac{\partial\mu}{\partial\mathbf{n}} ds = 0. \tag{2.9}
$$

To this end, we would like to propose an accurate and efficient numerical scheme to preserve the properties of the total energy dissipation and mass conservation. Thus, the numerical results produced by the numerical scheme would be physically consistent.

Now, we can construct a first-order discrete numerical scheme by the semi-implicit backward Euler's method with a uniform time step $\Delta t > 0$:

$$
\frac{\phi^{n+1}-\phi^n}{\Delta t} = \nabla\cdot(M^n\nabla\mu^{n+1}), \tag{2.10}
$$

$$
\mu^{n+1} = (\phi^n)^3 - \phi^{n+1} - \varepsilon^2\Delta\phi^{n+1}, \tag{2.11}
$$

with the following boundary conditions:

$$
\frac{\phi^{n+1}-\phi^n}{\Delta t} = -\eta\left[\varepsilon\frac{\partial\phi^{n+1}}{\partial\mathbf{n}} + \frac{\sqrt{2}}{2}\big((\phi^n)^2-1\big)\cos\theta_s\right], \quad \frac{\partial\mu^{n+1}}{\partial\mathbf{n}} = 0, \qquad \text{on } \Gamma_w, \tag{2.12}
$$

$$
\frac{\partial\phi^{n+1}}{\partial\mathbf{n}} = 0, \quad \frac{\partial\mu^{n+1}}{\partial\mathbf{n}} = 0, \qquad \text{on } \partial\Omega\backslash\Gamma_w, \tag{2.13}
$$

where $M^n = M(\phi^n)$ and ϕ^n is the approximation of ϕ at the time $t = t^n = n\Delta t$.

It is easy to prove that the above semi-implicit scheme (2.10)-(2.11) with boundary conditions (2.12)-(2.13) satisfies the conservation of total mass, but does not satisfy the energy dissipation. Moreover, this scheme has only first-order accuracy in time. From the numerical perspective, one main challenge in the numerical approximation is how to design unconditionally energy-stable schemes which keep the energy dissipative. The preservation of the energy dissipation law is particularly important, and is critical to precluding the nonphysical numerical solutions. Next, based on the IEQ method, we will construct a class of first- and second-order linear uniquely solvable numerical schemes, that satisfy the properties of energy dissipation and total mass conservation.

3 An efficient, unconditionally energy-stable scheme

For convince of presentation, we denote the inner product between functions $f(\mathbf{x})$ and $g(\mathbf{x})$ in $L^2(\Omega)$ and $L^2(\Gamma_w)$ space, respectively,

$$
(f(\mathbf{x}),g(\mathbf{x})) = \int_\Omega f(\mathbf{x})g(\mathbf{x})d\mathbf{x}, \qquad \langle f(\mathbf{x}),g(\mathbf{x})\rangle = \int_{\Gamma_w} f(\mathbf{x})g(\mathbf{x})ds, \tag{3.1}
$$

and the corresponding L^2-norm of functions $f(\mathbf{x})$ are, respectively,

$$\|f\|=(f,f)^{\frac{1}{2}}, \qquad \|f\|_w=\langle f,f\rangle^{\frac{1}{2}}. \tag{3.2}$$

We rewrite the total free energy functional W in (2.1) as

$$W[\phi]=\int_\Omega \frac{1}{2}\left(\varepsilon^2|\nabla\phi|^2+\beta\phi^2\right)d\mathbf{x}+\int_{\Gamma_w}\frac{\varepsilon\cos\theta_s}{3\sqrt{2}}(\phi^3-3\phi)ds+\int_\Omega\frac{1}{4}(\phi^2-1-\beta)^2d\mathbf{x}, \tag{3.3}$$

where β is a positive constant to be chosen to ensure that the integrand in the third term of (3.3) is positive, and we have already dropped a constant term in (2.1). We denote

$$g(\phi):\triangleq\frac{\varepsilon\cos\theta_s}{3\sqrt{2}}(\phi^3-3\phi), \qquad h(\phi):\triangleq\frac{1}{4}(\phi^2-1-\beta)^2. \tag{3.4}$$

It should be noted that, $g(\phi)\geq-\frac{\sqrt{2}}{3}\varepsilon$ and $h(\phi)\geq\frac{1}{4}\beta^2$ when $|\phi|\leq 1$, and $g(\phi)$ and $h(\phi)$ are bounded from below. By making use of the key idea of the IEQ approach [57,74], we reformulate the above integrands as two quadratic functions through the corresponding newly-defined variables, respectively. More precisely, we first define two auxiliary functions $p(\phi)$ and $q(\phi)$ as

$$p(\phi):\triangleq\sqrt{g(\phi)+C_0}, \qquad q(\phi):\triangleq\sqrt{h(\phi)}, \tag{3.5}$$

where C_0 is a constant to be chosen in order to ensure that the integrand $g(\phi)+C_0$ is positive. By some simple calculations, we can obtain the H^{-1}-gradient flow of the above energy functional with respect to the variables ϕ, μ, p and q as:

$$\frac{\partial\phi}{\partial t}=\nabla\cdot(M(\phi)\nabla\mu), \tag{3.6}$$

$$\mu=-\varepsilon^2\Delta\phi+\beta\phi+\frac{q}{\sqrt{h(\phi)}}h'(\phi), \tag{3.7}$$

$$\frac{\partial q}{\partial t}=\frac{1}{2\sqrt{h(\phi)}}h'(\phi)\frac{\partial\phi}{\partial t}, \tag{3.8}$$

subject to the following dynamic contact line boundary conditions:

$$\frac{\partial\phi}{\partial t}=-\eta\left(\varepsilon^2\frac{\partial\phi}{\partial\mathbf{n}}+\frac{p(\phi)}{\sqrt{g(\phi)+C_0}}g'(\phi)\right), \quad \frac{\partial\mu}{\partial\mathbf{n}}=0, \qquad \text{on } \Gamma_w, \tag{3.9}$$

$$\frac{\partial\phi}{\partial\mathbf{n}}=0, \quad \frac{\partial\mu}{\partial\mathbf{n}}=0, \qquad \text{on } \partial\Omega\backslash\Gamma_w, \tag{3.10}$$

with

$$\frac{\partial p}{\partial t}=\frac{1}{2\sqrt{g(\phi)+C_0}}g'(\phi)\frac{\partial\phi}{\partial t}, \tag{3.11}$$

where $M(\phi)$ is a phase function-dependent diffusive mobility defined before, and the constant $\eta(>0)$ represents the contact line mobility. It is easy to prove that the above governing equation also admits the total free energy dissipation and the mass conservation properties in terms of the new variable p, q, ϕ, μ.

In the following, we will develop the linearly, first-order and second-order, unconditionally energy-stable, numerical schemes for the time-stepping of the reformulated system (3.6)-(3.11).

3.1 First-order scheme

We now propose a semi-implicit first-order time-stepping numerical scheme for solving the above system, in which the time derivative is discretized by the backward Euler method (we label the scheme as IEQ/BDF1), i.e.

$$\frac{\phi^{n+1}-\phi^n}{\Delta t}=\nabla\cdot(M^n\nabla\mu^{n+1}), \tag{3.12}$$

$$\mu^{n+1}=-\varepsilon^2\Delta\phi^{n+1}+\beta\phi^{n+1}+\frac{q^{n+1}}{q^n}h'(\phi^n), \tag{3.13}$$

$$q^{n+1}-q^n=\frac{1}{2q^n}h'(\phi^n)(\phi^{n+1}-\phi^n), \tag{3.14}$$

subject to the following boundary conditions

$$\frac{\phi^{n+1}-\phi^n}{\Delta t}=-\eta\left(\varepsilon^2\frac{\partial\phi^{n+1}}{\partial\mathbf{n}}+\frac{p^{n+1}}{p^n}g'(\phi^n)\right),\quad \frac{\partial\mu^{n+1}}{\partial\mathbf{n}}=0,\qquad \text{on } \Gamma_w, \tag{3.15}$$

$$\frac{\partial\phi^{n+1}}{\partial\mathbf{n}}=0,\quad \frac{\partial\mu^{n+1}}{\partial\mathbf{n}}=0,\qquad \text{on } \partial\Omega\backslash\Gamma_w, \tag{3.16}$$

with

$$p^{n+1}-p^n=\frac{1}{2p^n}g'(\phi^n)(\phi^{n+1}-\phi^n), \tag{3.17}$$

where Δt denotes the time step and $t^n=n\Delta t$ for $n=0,\cdots,N$ with $T=N\Delta t$, $M^n=M(\phi^n)$, $p^n=p(\phi^n)$ and $q^n=q(\phi^n)$.

Next, we show that how the numerical scheme (3.12)-(3.14) coupled with the boundary conditions (3.15)-(3.16) are efficiently implemented. From Eqs. (3.14) and (3.17), we obtain

$$q^{n+1}=b^n\phi^{n+1}+(q^n-b^n\phi^n),\quad \text{where}\quad b^n:\triangleq\frac{h'(\phi^n)}{2q^n}, \tag{3.18}$$

$$p^{n+1}=a^n\phi^{n+1}+(p^n-a^n\phi^n),\quad \text{where}\quad a^n:\triangleq\frac{g'(\phi^n)}{2p^n}. \tag{3.19}$$

Then, we can reformulate the above system as follows

$$\phi^{n+1}-\Delta t\nabla\cdot(M^n\nabla\mu^{n+1})=\phi^n, \tag{3.20}$$

$$[\varepsilon^2\Delta-\beta-2(b^n)^2]\phi^{n+1}+\mu^{n+1}=2b^n(q^n-b^n\phi^n), \tag{3.21}$$

with the following boundary conditions

$$\Delta t\eta\varepsilon^2\frac{\partial\phi^{n+1}}{\partial\mathbf{n}}+[1+2\Delta t\eta(a^n)^2]\phi^{n+1}=f_0^n,\quad \frac{\partial\mu^{n+1}}{\partial\mathbf{n}}=0,\qquad \text{on } \Gamma_w, \tag{3.22}$$

$$\frac{\partial\phi^{n+1}}{\partial\mathbf{n}}=0,\quad \frac{\partial\mu^{n+1}}{\partial\mathbf{n}}=0,\qquad \text{on } \partial\Omega\backslash\Gamma_w, \tag{3.23}$$

where $f_0^n:\triangleq\phi^n-2\Delta t\eta a^n(p^n-a^n\phi^n)$. Therefore, we can solve ϕ^{n+1} and μ^{n+1} directly from (3.20) and (3.21) with the boundary conditions (3.22)-(3.23). Once we obtain ϕ^{n+1}, the q^{n+1} and p^{n+1} are automatically obtained by using (3.18) and (3.19), respectively. Therefore, the newly introduced variables p and q, in fact, do not involve in any extra computational costs.

For the IEQ/BDF1 scheme (3.12)-(3.14) with the boundary conditions (3.15)-(3.16), we can rigorously prove the well-posedness of the solution, and furthermore, we also can prove that the solution has the properties of the mass conservation and total free energy dissipation during the evolution.

Theorem 3.1 (Well-posedness)**.** *For the regularized mobility $M(\phi)\geq\varepsilon_M>0$, the linear system* (3.12)-(3.17) *(or* (3.20)-(3.23)*) admits a unique solution in $H^1(\Omega)$.*

Proof. Let $\alpha_0=\frac{1}{|\Omega|}\int_\Omega\phi^0d\mathbf{x}$, $\beta_\mu=\frac{1}{|\Omega|}\int_\Omega\mu^{n+1}d\mathbf{x}$, and we define

$$\phi=\phi^{n+1}-\alpha_0,\qquad \mu=\mu^{n+1}-\beta_\mu, \tag{3.24}$$

and $H_0^1(\Omega)=\{u|u\in H^1(\Omega),\int_\Omega ud\mathbf{x}=0\}$. Then, the variational formulation (or weak form) for (3.20)-(3.23) can be written as the following system with unknown variables $\mu,\phi\in H_0^1(\Omega)$,

$$\begin{cases}(\phi,\varphi)+\Delta t(M^n\nabla\mu,\nabla\varphi)=(\phi^n-\alpha_0,\varphi),\\ \varepsilon^2(\nabla\phi,\nabla\psi)+([\beta+2(b^n)^2]\phi,\psi)+\frac{1}{\Delta t\eta}\langle\phi,\psi\rangle+\langle 2(a^n)^2\phi,\psi\rangle-(\mu,\psi)=b_2,\end{cases}\quad\text{in } \Omega, \tag{3.25}$$

for any $\varphi,\psi\in H_0^1(\Omega)$, where

$$b_2:\triangleq(2b^n[b^n(\phi^n-\alpha_0)-q^n],\psi)+\langle 2a^n[a^n(\phi^n-\alpha_0)-p^n],\psi\rangle+\frac{1}{\Delta t\eta}\langle\phi^n-\alpha_0,\psi\rangle. \tag{3.26}$$

For convenience, we express the above linear system (3.25) as

$$(\mathbb{A}\mathbf{X},\mathbf{Y})=(\mathbb{B},\mathbf{Y}), \tag{3.27}$$

where $\mathbf{X}=(\mu,\phi)^T$, $\mathbf{Y}=(\varphi,\psi)^T$ and $\mathbf{X},\mathbf{Y}\in(H_0^1,H_0^1)(\Omega)$.

For any $\mathbf{X}=(\mu,\phi)^T$ and $\mathbf{Y}=(\varphi,\psi)^T$ with $\mathbf{X},\mathbf{Y}\in(H_0^1,H_0^1)(\Omega)$, we have

$$(\mathbb{A}\mathbf{X},\mathbf{Y})\leq C_1(\|\phi\|_{H^1}+\|\mu\|_{H^1})(\|\psi\|_{H^1}+\|\varphi\|_{H^1}), \tag{3.28}$$

by using the trace theorem, where C_1 is a constant depending on $\Delta t,\varepsilon,\beta,\eta,\|M^n\|_\infty,\|a^n\|_\infty$, $\|b^n\|_\infty$. Thus, the bilinear form $(\mathbb{A}\mathbf{X},\mathbf{Y})$ is bounded.

It is easy to derive that

$$\begin{aligned}(\mathbb{A}\mathbf{X},\mathbf{X})&=\Delta t(M^n\nabla\mu,\nabla\mu)+\varepsilon^2(\nabla\phi,\nabla\phi)+([\beta+2(b^n)^2]\phi,\phi)+\frac{1}{\Delta t\eta}\langle\phi,\phi\rangle+\langle 2(a^n)^2\phi,\phi\rangle\\&=\Delta t\|\sqrt{M^n}\nabla\mu\|^2+\varepsilon^2\|\nabla\phi\|^2+\beta\|\phi\|^2+2\|b^n\phi\|^2+\frac{1}{\Delta t\eta}\|\phi\|_w^2+2\|a^n\phi\|_w^2\\&\geq C_2\left(\|\phi\|_{H^1}^2+\|\mu\|_{H^1}^2\right),\end{aligned} \tag{3.29}$$

from Poincaré inequality (since $\int_\Omega\phi d\mathbf{x}=\int_\Omega\mu d\mathbf{x}=0$), where C_2 is a positive constant depending on $\Delta t,\varepsilon,\beta,\eta,\varepsilon_M,|a^n|_{\min},|b^n|_{\min}$. Thus the bilinear form $(\mathbb{A}\mathbf{X},\mathbf{Y})$ is coercive.

By applying the Lax-Milgram theorem, we conclude that the linear system (3.25) admits a unique solution in $H_0^1(\Omega)$. Namely, the linear system (3.20)-(3.23) admits a unique solution in $H^1(\Omega)$. □

Theorem 3.2 (Mass conservation)**.** *The first-order linear scheme* (3.12)-(3.14) *with the boundary conditions* (3.15)-(3.16) *ensures that the total mass $m(t)$ is conserved during the evolution, i.e.*

$$\int_\Omega\phi^{n+1}d\mathbf{x}=\int_\Omega\phi^n d\mathbf{x}=\cdots=\int_\Omega\phi^0 d\mathbf{x}. \tag{3.30}$$

Proof. From Eq. (3.12), we obtain

$$\begin{aligned}\int_\Omega\phi^{n+1}d\mathbf{x}&=\int_\Omega\phi^n d\mathbf{x}+\Delta t\int_\Omega\nabla\cdot(M^n\nabla\mu^{n+1})d\mathbf{x}\\&=\int_\Omega\phi^n d\mathbf{x}+\Delta t\int_{\partial\Omega}M^n\frac{\partial\mu^{n+1}}{\partial\mathbf{n}}ds\\&=\int_\Omega\phi^n d\mathbf{x}=\int_\Omega\phi^{n-1}d\mathbf{x}=\cdots=\int_\Omega\phi^0 d\mathbf{x}.\end{aligned} \tag{3.31}$$

Here we use the boundary conditions $(3.15)_2$ and $(3.16)_2$, then the theorem is proved. □

Theorem 3.3 (Energy dissipation)**.** *The first-order linear scheme* (3.12)-(3.14) *with the boundary conditions* (3.15)-(3.16) *is unconditionally energy-stable, i.e., satisfies the following discrete energy dissipation law:*

$$\begin{aligned}W^{n+1}-W^n=&-\left[\frac{\varepsilon^2}{2}\|\nabla\phi^{n+1}-\nabla\phi^n\|^2+\frac{\beta}{2}\|\phi^{n+1}-\phi^n\|^2+\|q^{n+1}-q^n\|^2+\|p^{n+1}-p^n\|_w^2\right]\\&-\frac{1}{\eta\Delta t}\|\phi^{n+1}-\phi^n\|_w^2-\Delta t\|\sqrt{M^n}\nabla\mu^{n+1}\|^2\leq 0,\end{aligned} \tag{3.32}$$

where

$$W^n=\int_\Omega \frac{1}{2}\left[\varepsilon^2|\nabla\phi^n|^2+\beta(\phi^n)^2\right]d\mathbf{x}+\int_{\Gamma_w}\frac{\varepsilon\cos\theta_s}{3\sqrt{2}}\left[(\phi^n)^3-3\phi^n\right]ds+\int_\Omega\frac{1}{4}\left[(\phi^n)^2-1-\beta\right]^2 d\mathbf{x}. \tag{3.33}$$

Proof. Taking the L^2-inner products of (3.12)-(3.14), $(3.15)_1$ and (3.17) with μ^{n+1}, $\frac{\phi^{n+1}-\phi^n}{\Delta t}$, $2q^{n+1}$, $-\frac{1}{\eta}\frac{\phi^{n+1}-\phi^n}{\Delta t}$ and $2p^{n+1}$, respectively, we obtain

$$\left(\frac{\phi^{n+1}-\phi^n}{\Delta t},\mu^{n+1}\right)=\left(\nabla\cdot(M^n\nabla\mu^{n+1}),\mu^{n+1}\right)=-\left(M^n\nabla\mu^{n+1},\nabla\mu^{n+1}\right), \tag{3.34}$$

$$\begin{aligned}\left(\mu^{n+1},\frac{\phi^{n+1}-\phi^n}{\Delta t}\right)&=\left(-\varepsilon^2\Delta\phi^{n+1}+\beta\phi^{n+1}+\frac{q^{n+1}}{q^n}h'(\phi^n),\frac{\phi^{n+1}-\phi^n}{\Delta t}\right)\\&=-\frac{\varepsilon^2}{\Delta t}\left\langle\frac{\partial\phi^{n+1}}{\partial\mathbf{n}},\phi^{n+1}-\phi^n\right\rangle+\frac{\varepsilon^2}{\Delta t}\left(\nabla\phi^{n+1},\nabla(\phi^{n+1}-\phi^n)\right)\\&\quad+\frac{\beta}{\Delta t}\left(\phi^{n+1},\phi^{n+1}-\phi^n\right)+\frac{1}{\Delta t}\left(\frac{q^{n+1}}{q^n}h'(\phi^n),\phi^{n+1}-\phi^n\right),\end{aligned} \tag{3.35}$$

$$\left(q^{n+1}-q^n,2q^{n+1}\right)=\left(\frac{q^{n+1}}{q^n}h'(\phi),\phi^{n+1}-\phi^n\right), \tag{3.36}$$

$$\left\langle\frac{\phi^{n+1}-\phi^n}{\Delta t},-\frac{1}{\eta}\frac{\phi^{n+1}-\phi^n}{\Delta t}\right\rangle=\frac{\varepsilon^2}{\Delta t}\left\langle\frac{\partial\phi^{n+1}}{\partial\mathbf{n}},\phi^{n+1}-\phi^n\right\rangle+\frac{1}{\Delta t}\left\langle\frac{p^{n+1}}{p^n}g'(\phi^n),\phi^{n+1}-\phi^n\right\rangle, \tag{3.37}$$

$$\left\langle p^{n+1}-p^n,2p^{n+1}\right\rangle=\left\langle\frac{p^{n+1}}{p^n}g'(\phi),\phi^{n+1}-\phi^n\right\rangle. \tag{3.38}$$

here we use the boundary conditions (3.15)-(3.16). Applying the following identities

$$2(u-v,u)=\|u\|^2-\|v\|^2+\|u-v\|^2, \tag{3.39}$$

we obtain

$$\begin{aligned}&-\Delta t\left(M^n\nabla\mu^{n+1},\nabla\mu^{n+1}\right)-\frac{1}{\eta\Delta t}\left\langle\phi^{n+1}-\phi^n,\phi^{n+1}-\phi^n\right\rangle\\=&\varepsilon^2\left(\nabla\phi^{n+1},\nabla(\phi^{n+1}-\phi^n)\right)+\beta\left(\phi^{n+1},\phi^{n+1}-\phi^n\right)\\&+\left(q^{n+1}-q^n,2q^{n+1}\right)+\left\langle p^{n+1}-p^n,2p^{n+1}\right\rangle\\=&\frac{1}{2}\varepsilon^2\left(\|\nabla\phi^{n+1}\|^2-\|\nabla\phi^n\|^2+\|\nabla\phi^{n+1}-\nabla\phi^n\|^2\right)\\&+\frac{1}{2}\beta\left(\|\phi^{n+1}\|^2-\|\phi^n\|^2+\|\phi^{n+1}-\phi^n\|^2\right)+\left(\|q^{n+1}\|^2-\|q^n\|^2+\|q^{n+1}-q^n\|^2\right)\\&+\left(\|p^{n+1}\|_w^2-\|p^n\|_w^2+\|p^{n+1}-p^n\|_w^2\right).\end{aligned} \tag{3.40}$$

Equivalently, the above equation can be rewritten as

$$W^{n+1}-W^n=-\left[\frac{\varepsilon^2}{2}\|\nabla\phi^{n+1}-\nabla\phi^n\|^2+\frac{\beta}{2}\|\phi^{n+1}-\phi^n\|^2+\|q^{n+1}-q^n\|^2+\|p^{n+1}-p^n\|_w^2\right]$$
$$-\frac{1}{\eta\Delta t}\|\phi^{n+1}-\phi^n\|_w^2-\Delta t\|\sqrt{M^n}\nabla\mu^{n+1}\|^2\leq 0. \tag{3.41}$$

Therefore, the theorem has been proved. □

3.2 Second-order scheme

In the following, we propose a second-order time-stepping numerical scheme for solving the system (3.6)-(3.11), in which the time derivative is discretized by the second-order Adams-Bashforth backward differentiation formula (we label this scheme as IEQ/BDF2):

$$\frac{3\phi^{n+1}-4\phi^n+\phi^{n-1}}{2\Delta t}=\nabla\cdot(\bar{M}^{n+1}\nabla\mu^{n+1}), \tag{3.42}$$

$$\mu^{n+1}=-\varepsilon^2\Delta\phi^{n+1}+\beta\phi^{n+1}+\frac{q^{n+1}}{\bar{q}^{n+1}}h'(\bar{\phi}^{n+1}), \tag{3.43}$$

$$3q^{n+1}-4q^n+q^{n-1}=\frac{1}{2\bar{q}^{n+1}}h'(\bar{\phi}^{n+1})(3\phi^{n+1}-4\phi^n+\phi^{n-1}), \tag{3.44}$$

subject to the following boundary conditions

$$\frac{3\phi^{n+1}-4\phi^n+\phi^{n-1}}{2\Delta t}=-\eta\left(\varepsilon^2\frac{\partial\phi^{n+1}}{\partial\mathbf{n}}+\frac{p^{n+1}}{\bar{p}^{n+1}}g'(\bar{\phi}^{n+1})\right),\quad \frac{\partial\mu^{n+1}}{\partial\mathbf{n}}=0,\quad \text{on } \Gamma_w, \tag{3.45}$$

$$\frac{\partial\phi^{n+1}}{\partial\mathbf{n}}=0,\quad \frac{\partial\mu^{n+1}}{\partial\mathbf{n}}=0,\quad \text{on } \partial\Omega\backslash\Gamma_w, \tag{3.46}$$

with

$$3p^{n+1}-4p^n+p^{n-1}=\frac{1}{2\bar{p}^{n+1}}g'(\bar{\phi}^{n+1})(3\phi^{n+1}-4\phi^n+\phi^{n-1}), \tag{3.47}$$

where $\bar{M}^{n+1}=M(\bar{\phi}^{n+1})$, $\bar{p}^{n+1}=p(\bar{\phi}^{n+1})$ and $\bar{q}^{n+1}=q(\bar{\phi}^{n+1})$, $\bar{\phi}^{n+1}=2\phi^n-\phi^{n-1}$ is the explicit approximation of $\phi(t^{n+1})$ with local truncation error of $\mathcal{O}(\Delta t^2)$.

Next, we describe how the scheme (3.42)-(3.44) with the boundary conditions (3.45)-(3.46) can be efficiently implemented. From Eqs. (3.44) and (3.47), we obtain

$$q^{n+1}=\bar{b}^{n+1}\phi^{n+1}+\frac{1}{3}\left[(4q^n-q^{n-1})-\bar{b}^{n+1}(4\phi^n-\phi^{n-1})\right],\quad \text{where } \bar{b}^{n+1}:\triangleq\frac{h'(\bar{\phi}^{n+1})}{2\bar{q}^{n+1}}, \tag{3.48}$$

$$p^{n+1}=\bar{a}^{n+1}\phi^{n+1}+\frac{1}{3}\left[(4p^n-p^{n-1})-\bar{a}^{n+1}(4\phi^n-\phi^{n-1})\right],\quad \text{where } \bar{a}^{n+1}:\triangleq\frac{g'(\bar{\phi}^{n+1})}{2\bar{p}^{n+1}}. \tag{3.49}$$

Then, we can reformulate the above system as follows

$$3\phi^{n+1}-2\Delta t\nabla\cdot(\bar{M}^{n+1}\nabla\mu^{n+1})=4\phi^n-\phi^{n-1}, \tag{3.50}$$

$$[\varepsilon^2\Delta-\beta-2(\bar{b}^{n+1})^2]\phi^{n+1}+\mu^{n+1}=\frac{2}{3}\bar{b}^{n+1}\Big[(4q^n-q^{n-1})-\bar{b}^{n+1}(4\phi^n-\phi^{n-1})\Big], \tag{3.51}$$

with the following boundary conditions

$$2\Delta t\eta\varepsilon^2\frac{\partial\phi^{n+1}}{\partial\mathbf{n}}+[3+4\Delta t\eta(\bar{a}^{n+1})^2]\phi^{n+1}=\bar{f}_0^n,\quad \frac{\partial\mu^{n+1}}{\partial\mathbf{n}}=0,\quad \text{on } \Gamma_w, \tag{3.52}$$

$$\frac{\partial\phi^{n+1}}{\partial\mathbf{n}}=0,\quad \frac{\partial\mu^{n+1}}{\partial\mathbf{n}}=0,\quad \text{on } \partial\Omega\backslash\Gamma_w, \tag{3.53}$$

where $\bar{f}_0^n:\triangleq(4\phi^n-\phi^{n-1})-\frac{4}{3}\Delta t\eta\bar{a}^{n+1}\left[(4p^n-p^{n-1})-\bar{a}^{n+1}(4\phi^n-\phi^{n-1})\right]$. Therefore, we can solve ϕ^{n+1} and μ^{n+1} directly from (3.50)-(3.51) with the boundary conditions (3.52)-(3.53). Once we obtain ϕ^{n+1}, the two unknown variables q^{n+1} and p^{n+1} are automatically obtained from (3.48) and (3.49), respectively.

For the IEQ/BDF2 scheme (3.42)-(3.44) with the boundary conditions (3.45)-(3.46), we can also rigorously prove the well-posedness, total mass conservation and energy dissipation.

Theorem 3.4 (Well-posedness)**.** *For the regularized mobility $M(\phi)\geq\varepsilon_M>0$, the linear system* (3.42)-(3.47) *admits a unique solution in $H^1(\Omega)$.*

Proof. The proof is similar to Theorem 3.1, thus we omit the details here. □

Theorem 3.5 (Mass conservation)**.** *The second order linear scheme* (3.42)-(3.44) *with the boundary conditions* (3.45)-(3.46) *ensures that the total mass $m(t)$ is conserved during the evolution, i.e.*

$$\int_\Omega\phi^{n+1}d\mathbf{x}=\int_\Omega\phi^n d\mathbf{x}=\cdots=\int_\Omega\phi^0 d\mathbf{x}. \tag{3.54}$$

Proof. From Eq. (3.42), we obtain

$$\int_\Omega(3\phi^{n+1}-4\phi^n+\phi^{n-1})d\mathbf{x}=2\Delta t\int_\Omega\nabla\cdot(\bar{M}^{n+1}\nabla\mu^{n+1})d\mathbf{x}=2\Delta t\int_{\partial\Omega}\bar{M}^{n+1}\frac{\partial\mu^{n+1}}{\partial\mathbf{n}}ds=0, \tag{3.55}$$

here we use the boundary conditions $(3.45)_2$ and $(3.46)_2$, then

$$\int_\Omega(\phi^{n+1}-\phi^n)d\mathbf{x}=\frac{1}{3}\int_\Omega(\phi^n-\phi^{n-1})d\mathbf{x}=\cdots=\frac{1}{3^n}\int_\Omega(\phi^1-\phi^0)d\mathbf{x}. \tag{3.56}$$

Since we solve for ϕ^1 through the first-order IEQ/BDF1 scheme (3.12)-(3.17), from Theorem 3.2, we obtain $\int_\Omega\phi^1 d\mathbf{x}=\int_\Omega\phi^0 d\mathbf{x}$. Therefore, one has $\int_\Omega(\phi^{n+1}-\phi^n)d\mathbf{x}=0$, and further

$$\int_\Omega\phi^{n+1}d\mathbf{x}=\int_\Omega\phi^n d\mathbf{x}=\cdots=\int_\Omega\phi^0 d\mathbf{x}. \tag{3.57}$$

The proof is completed. □

Theorem 3.6 (Energy dissipation)**.** *The second-order linear scheme* (3.42)-(3.44) *with the boundary conditions* (3.45)-(3.46) *is unconditionally energy-stable, i.e., satisfies the following discrete energy dissipation law:*

$$\begin{aligned} W^{n+1,n}-W^{n,n-1}=&-\left(\Delta t\|\sqrt{\bar{M}^{n+1}}\nabla\mu^{n+1}\|^2+\frac{1}{4\eta\Delta t}\|3\phi^{n+1}-4\phi^n+\phi^{n-1}\|_w^2\right.\\ &+\frac{\varepsilon^2}{4}\|\nabla\phi^{n+1}-2\nabla\phi^n+\nabla\phi^{n-1}\|^2+\frac{\beta}{4}\|\phi^{n+1}-2\phi^n+\phi^{n-1}\|^2\\ &\left.+\frac{\|q^{n+1}-2q^n+q^{n-1}\|^2}{2}+\frac{\|p^{n+1}-2p^n+p^{n-1}\|_w^2}{2}\right)\leq 0, \end{aligned} \tag{3.58}$$

where

$$\begin{aligned} W^{n,n-1}=&\frac{\varepsilon^2}{2}\left(\frac{\|\nabla\phi^n\|^2+\|2\nabla\phi^n-\nabla\phi^{n-1}\|^2}{2}\right)+\frac{\beta}{2}\left(\frac{\|\phi^n\|^2+\|2\phi^n-\phi^{n-1}\|^2}{2}\right)\\ &+\left(\frac{\|q^n\|^2+\|2q^n-q^{n-1}\|^2}{2}\right)+\left(\frac{\|p^n\|_w^2+\|2p^n-p^{n-1}\|_w^2}{2}\right). \end{aligned} \tag{3.59}$$

Proof. Similar to the proof of Theorem 3.3, and by taking the L^2-inner products of (3.42)-(3.44), $(3.45)_1$ and (3.47) with μ^{n+1}, $\frac{3\phi^{n+1}-4\phi^n+\phi^{n-1}}{2\Delta t}$, $2q^{n+1}$, $-\frac{1}{\eta}\frac{3\phi^{n+1}-4\phi^n+\phi^{n-1}}{2\Delta t}$ and $2p^{n+1}$, we can obtain the conclusion. □

It is also straightforward to develop the second-order Crank-Nicolson scheme for solving the above system. To simplify the presentation, we have only discussed the temporal discretization for the above numerical schemes. However, since the stability proofs of IEQ schemes are all variational, these results can be carried over to fully discretized IEQ schemes with Galerkin finite element methods, spectral methods or finite difference methods with summation by parts. The local truncation error of the proposed schemes can be readily derived via Taylor series expansion by assuming that the classical solutions of the PDE system have enough regularity. We omit the details here for brevity.

4 Numerical results & discussion

In this section, we present ample numerical experiments to validate the theoretical results of the proposed numerical scheme, and demonstrate the accuracy and high efficiency of the scheme for investigating the kinetic evolution of solid-state dewetting.

Let $\Omega=[a,b]\times[c,d]$ be a rectangular computational domain and denote mesh sizes $\Delta x=\frac{b-a}{N_x}$ and $\Delta y=\frac{d-c}{N_y}$, with N_x and N_y the mesh grid numbers along the x and y directions, respectively. Then, we can use the second-order central difference scheme to discretize spatial derivatives, and we use the composite trapezoidal rules to calculate the numerical integration which is involved in the numerical calculations (e.g., calculating the total mass and total free energy).

If not explicitly specified, we use the initial shape as a rectangle, which is located in $[-0.5,0.5]\times[0,0.2]$ in the computational domain. The time step $\Delta t=0.01$ and the computational parameters are chosen as $\beta=5$, $C_0=1$, $\eta=100$, $\varepsilon_M=10^{-8}$, and the diffusive mobility function $M(\phi)=|1-\phi^2|+\varepsilon_M$. The numerical simulations were terminated when the shape of the film arrives at its equilibrium state, which is numerically defined when the discrete L^2-norm $\|\phi^{n+1}-\phi^n\|_{l^2}<10^{-6}$ is first achieved during numerical simulations.

Example 4.1. (Convergence rates) We consider six different time steps $\Delta t=0.005\times 2^{-j}$, where $j=1,2,\cdots,6$, and the corresponding numerical solutions are labeled as ϕ_j $(j=1,2,\cdots,6)$ (shown in Tables 1-2), respectively. The initial value of the phase field variable is chosen to be

$$\phi(x,y,0)=\tanh\left(\frac{0.25-\sqrt{x^2+y^2}}{\sqrt{2}\varepsilon}\right), \tag{4.1}$$

and the mesh size $\Delta x=\Delta y=0.004$, the Young contact angle $\theta_s=\frac{3\pi}{4}$, and the interface width parameter $\varepsilon=0.1$.

The numerical errors at two different times $t=0.05$ and $t=0.1$ for IEQ/BDF1 and IEQ/BDF2 schemes are shown in Table 1-2, respectively. As expected, we can clearly observe the first-order accuracy in time for the IEQ/BDF1 scheme, and second-order accuracy for the IEQ/BDF2 scheme.

Table 1: (Example 4.1) Errors and convergence rates in l^2- and $l^\infty-$norms by using IEQ/BDF1 scheme.

	$t=0.05$				$t=0.1$			
j	$\|\phi_{j+1}-\phi_j\|_{l^2}$	order	$\|\phi_{j+1}-\phi_j\|_{l^\infty}$	order	$\|\phi_{j+1}-\phi_j\|_{l^2}$	order	$\|\phi_{j+1}-\phi_j\|_{l^\infty}$	order
1	1.5343e-0	-	2.5060e-2	-	9.5921e-1	-	2.0513e-2	-
2	6.6878e-1	1.1980	1.1839e-2	1.0819	5.5490e-1	0.7896	1.2433e-2	0.7224
3	3.2022e-1	1.0624	6.1872e-3	0.9362	3.0455e-1	0.8656	6.8433e-3	0.8614
4	1.5924e-1	1.0079	3.1936e-3	0.9541	1.5993e-1	0.9292	3.5623e-3	0.9415
5	7.9756e-2	0.9976	1.6193e-3	0.9798	8.1950e-2	0.9647	1.8086e-3	0.9783

Table 2: (Example 4.1) Errors and convergence rates in l^2- and $l^\infty-$norms by using IEQ/BDF2 scheme.

	$t=0.05$				$t=0.1$			
j	$\|\phi_{j+1}-\phi_j\|_{l^2}$	order	$\|\phi_{j+1}-\phi_j\|_{l^\infty}$	order	$\|\phi_{j+1}-\phi_j\|_{l^2}$	order	$\|\phi_{j+1}-\phi_j\|_{l^\infty}$	order
1	1.4479e-1	-	2.7686e-3	-	7.2866e-2	-	1.7948e-3	-
2	3.9179e-2	1.8858	8.8680e-4	1.6425	2.0714e-2	1.8147	5.1074e-4	1.8131
3	1.0405e-2	1.9128	2.4134e-4	1.8776	5.4227e-3	1.9335	1.3129e-4	1.9598
4	2.6833e-3	1.9552	6.1773e-5	1.9660	1.3699e-3	1.9849	3.1035e-5	2.0808
5	6.8867e-4	1.9621	1.5309e-5	2.0126	3.5880e-4	1.9329	7.9402e-6	1.9667

Example 4.2. (Energy dissipation and mass conservation) We consider the Young contact angle $\theta_s = \frac{3\pi}{4}$ and the interface parameter $\varepsilon = 0.05$ with three different time step $\Delta t = 0.10$, 0.05, 0.01, respectively, the mesh size $\Delta x = \Delta y = 0.004$.

We first examine the temporal evolution of the total free energy by using these two schemes. As shown in Fig. 3(a), we clearly observe that all of the six temporal evolution curves about the total free energy decreases at all times, and the second-order IEQ/BDF2 scheme dissipate the total free energy more quickly than the first-order IEQ/BDF1 scheme. Furthermore, for the same scheme, the smaller the time step is, the faster the total free energy decreases. It demonstrates that the high-order and small time-stepping scheme is more accurate than the first-order and large time-stepping scheme, and also confirms that our proposed numerical schemes are unconditionally energy-stable. In addition, we also plot the total mass evolution curves in Fig. 3(b) by using three different time steps, i.e., $\Delta t = 0.10$, 0.05, 0.01, with IEQ/BDF1 and IEQ/BDF2 schemes, respectively, and we clearly observe that the proposed IEQ schemes ensure that the total mass is conserved during the evolution.

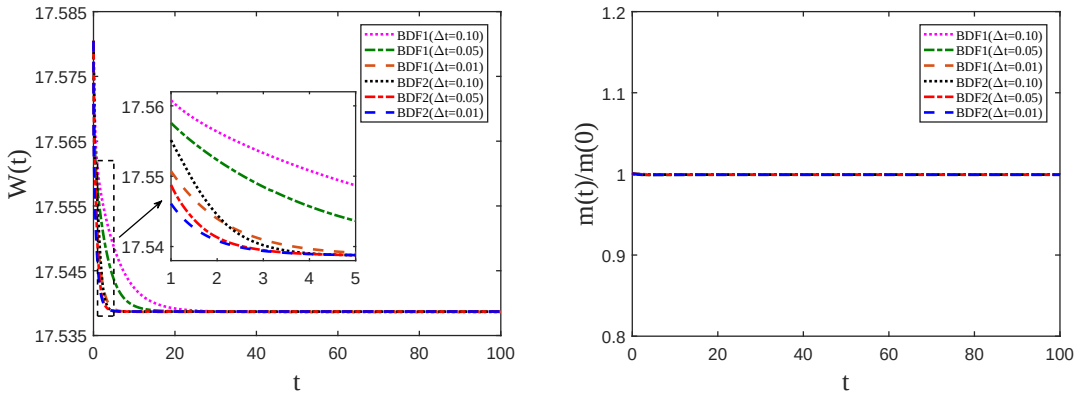

Figure 3: (Example 4.2) The temporal evolution of the total free energy (left) and the normalized total mass (right) under three different time steps $\Delta t = 0.1$, 0.05, 0.01 by using the numerical schemes IEQ/BDF1 and IEQ/BDF2, respectively.

Example 4.3. (Convergence of interface width parameter ε) We consider four different interface parameters ε=0.04, 0.03, 0.02, 0.01 under two different Young contact angles $\theta_s = \frac{3\pi}{4}, \frac{\pi}{4}$, and the corresponding mesh sizes $\Delta x = \Delta y = 0.004$, 0.003, 0.002, 0.001, respectively. The theoretical equilibrium states (shown in blue lines by Fig. 4) are determined by the Winterbottom construction [28,75].

By reducing the interface width parameters ε, the convergence results of the numerical equilibrium state to its theoretical equilibrium state (shown in blue lines) are shown in Fig. 4 under two different Young contact angles, $\theta_s = \frac{3\pi}{4}$ and $\theta_s = \frac{\pi}{4}$. We clearly observe that the numerical equilibrium shapes uniformly converge to the theoretical equilibrium shape, when the interface width parameter ε decreases from 0.04 to 0.01.

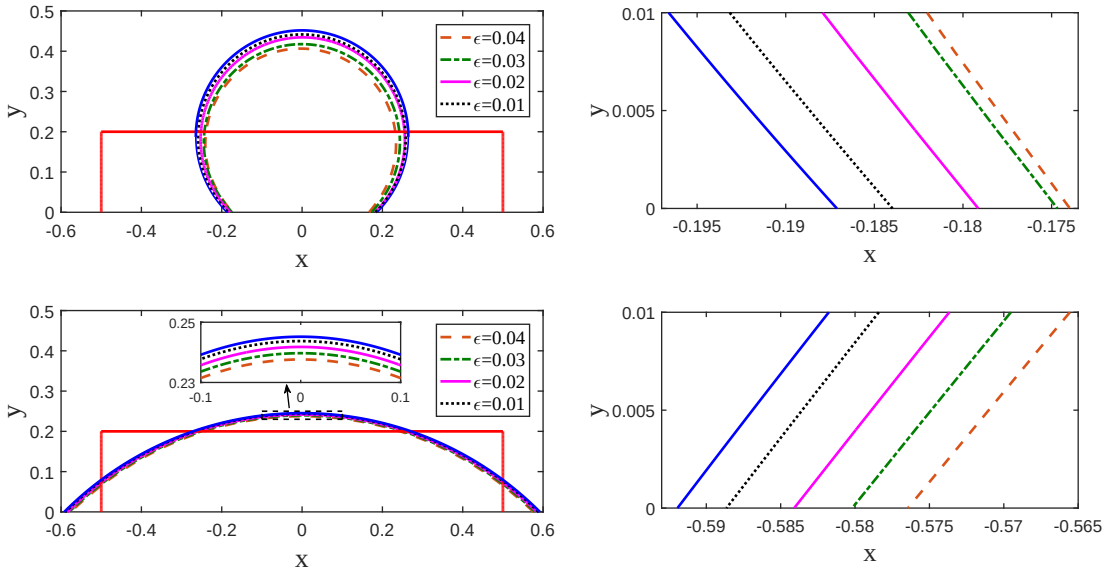

Figure 4: (Example 4.3) Convergence results to the theoretical equilibrium shapes (shown in blue lines) obtained by decreasing the parameter ε under the prescribe contact angels: $\theta_s = \frac{3\pi}{4}$ (top) and $\theta_s = \frac{\pi}{4}$ (bottom), where the initial state of the film is shown in red lines, and the right column depicts the zoomed-in pictures near the left contact points.

Example 4.4. (Effects of contact line mobility η) We consider four different contact line mobilities $\eta = 50$, 100, 150, 200 with the interface parameter $\varepsilon = 0.02$ under two different Young contact angles $\theta_s = \frac{3\pi}{4}, \frac{\pi}{4}$, respectively, the time step $\Delta t = 0.005$ and the mesh size $\Delta x = \Delta y = 0.002$.

The contact line mobility η determines the rate of relaxation of the dynamic contact angle θ to the equilibrium contact angle θ_s which satisfies the Young equation [26]. Note that in the phase-field model, because of the finite thickness of the interface width ε, in general the dynamic contact angle θ can not perfectly converge to θ_s (shown in Fig. 5). In general, for small η, the relaxation is very slow and the contact points move very slowly; on the other hand, if η is very large, the relaxation process occurs very quickly such that the dynamical contact angle θ quickly converges. Fig. 5 depicts the temporal evolution of the dynamic contact angle (measured by numerical solutions near the contact points) under four different contact line mobilities ($\eta = 50$, 100, 150, 200) with $\theta_s = \frac{3\pi}{4}, \frac{\pi}{4}$, respectively. As shown in this figure, the contact angle initially increases (for $\theta_s = \frac{3\pi}{4}$ case) or decreases (for $\theta_s = \frac{\pi}{4}$ case) very quickly from its initial value $\theta = \frac{\pi}{2}$ to a near steady-state value. Then, as the island approaches its equilibrium shape, the contact point slows and the dynamic contact angle gradually converges to an equilibrium value. Furthermore, when η increases to a critical value, there is no visual difference for the evolution curve of dynamic contact angles between $\eta = 150$ and $\eta = 200$. This is consistent with experimental and atomistic simulation observation of the triple junction drag effect on

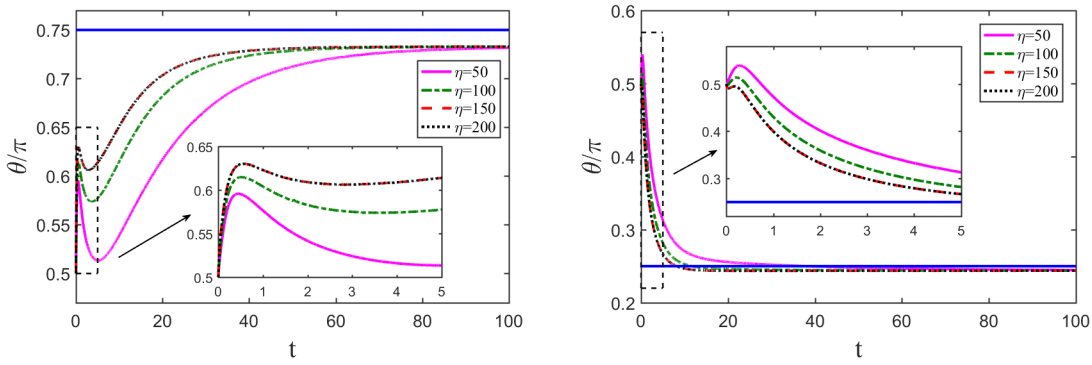

(a) $\theta_s=\frac{3\pi}{4}$ (b) $\theta_s=\frac{\pi}{4}$

Figure 5: (Example 4.4) The temporal evolution of the contact angle under four different contact line mobilities, where the blue lines show the Young contact angle θ_s.

dynamic triple junction angles in grain boundaries [76,77] and in contact lines of fluids on substrates [21,22].

Example 4.5. (Morphological evolution under different Young contact angles) We consider eight different Young contact angles $\theta_s=\pi$, $\frac{5\pi}{6}$, $\frac{3\pi}{4}$, $\frac{\pi}{2}$, $\frac{\pi}{3}$, $\frac{\pi}{4}$, $\frac{\pi}{6}$, 0 with the interface parameter $\varepsilon=0.04$, respectively, where the mesh size is chosen as $\Delta x=\Delta y=0.004$.

The evolution of the island towards its equilibrium shape is shown in Fig. 6 under several prescribed Young contact angle θ_s. From these figures, we clearly observe that the prescribed contact angle θ_s is rapidly achieved at the contact points so that the island evolves towards its equilibrium state. This includes the extreme cases of complete dewetting $\theta_s=\pi$ (the equilibrium is a full circle that touches the substrate at a point), complete wetting $\theta_s=0$ (the equilibrium is a continuous film) or any intermediate $\theta_s\in(0,\pi)$.

Example 4.6. (Hole dynamics) We assume that the initial film occupies the region $x\leq -0.05$ and $x\geq 0.05$, and it has a thickness of 0.1, and the interface parameter $\varepsilon=0.01$ and mesh size is $\Delta x=\Delta y=0.002$ under two different Young contact angle $\theta_s=\frac{5\pi}{6}$, $\frac{\pi}{6}$, respectively.

Fig. 7 shows the evolution of a thin film containing a small hole (that extends through the film to the substrate) at its center under two different prescribed contact angles $\theta_s=\frac{5\pi}{6}$ and $\theta_s=\frac{\pi}{6}$. For the $\theta_s=\frac{5\pi}{6}$ case (see Fig. 7(a)), the hole grows and eventually achieves the equilibrium circular shape. However, for $\theta_s=\frac{\pi}{6}$ (see Fig. 7(b)), the initial hole closes, the valley where the hole was located disappears and the film approaches a metastable flat morphology. The numerical results are consistent with the analysis in Ref. [78], and the numerical simulation by the semi-implicit numerical scheme in Ref. [16].

Example 4.7. (Effects of different degenerate mobilities) Finally, we investigate the effect of different degenerate mobilities on the kinetic evolution of solid-state dewetting. Here,

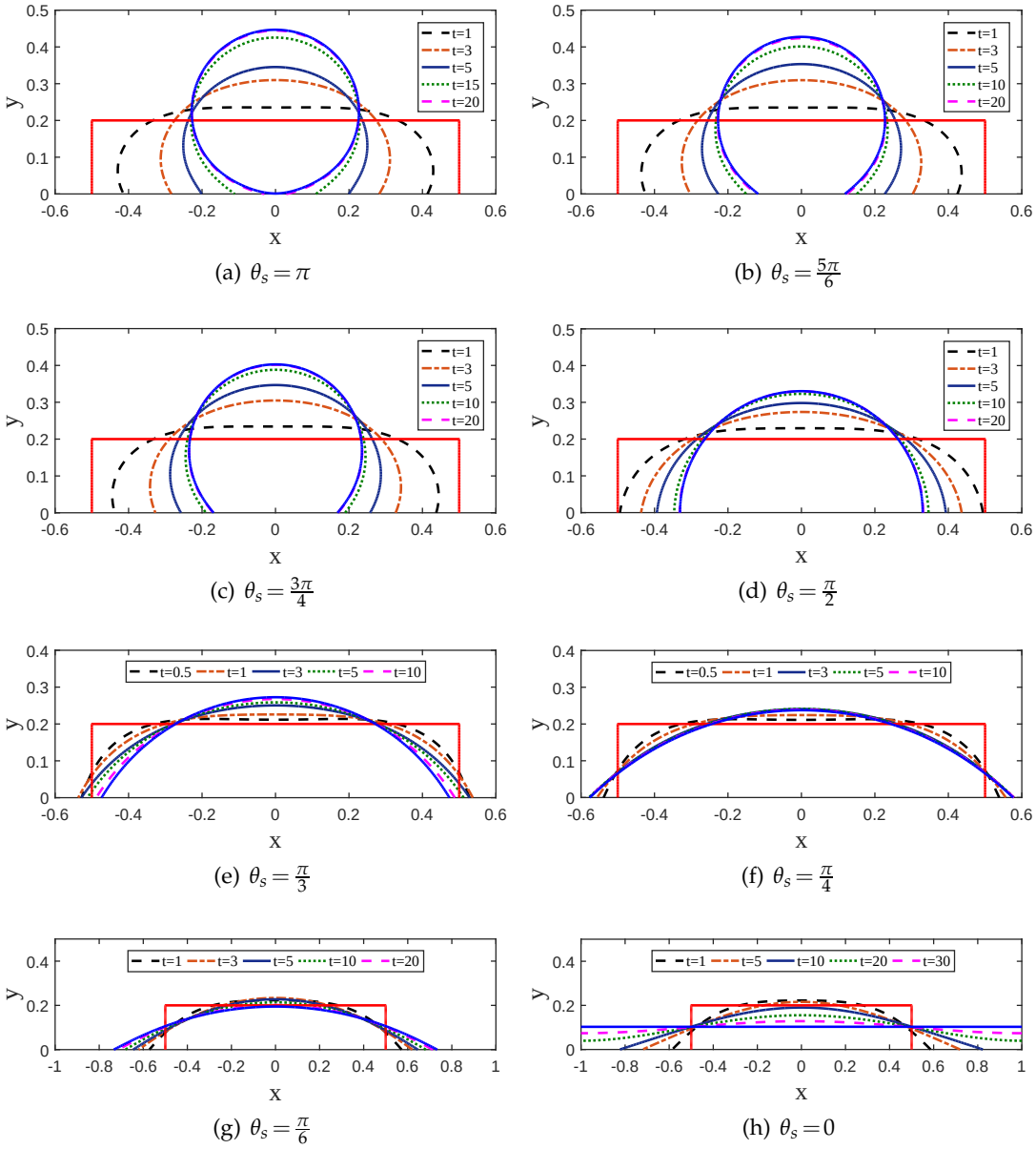

(a) $\theta_s=\pi$ (b) $\theta_s=\frac{5\pi}{6}$

(c) $\theta_s=\frac{3\pi}{4}$ (d) $\theta_s=\frac{\pi}{2}$

(e) $\theta_s=\frac{\pi}{3}$ (f) $\theta_s=\frac{\pi}{4}$

(g) $\theta_s=\frac{\pi}{6}$ (h) $\theta_s=0$

Figure 6: (Example 4.5) Several steps of the evolution of initially rectangular islands (shown in red) towards their equilibrium shapes (shown in blue) under eight different Young contact angels.

we consider two different degenerate mobility functions, i.e., $M_1(\phi)=|1-\phi^2|+\varepsilon_M$ and $M_2(\phi)=(1-\phi^2)^2+\varepsilon_M$. The initial shape of island films are chosen as: (1). a short island film (shown in Fig. 8), located in the region $[-0.5,0.5]\times[0,0.2]$; (2). a long island film (shown in Fig. 9), located in the region $[-1.3,1.3]\times[0,0.065]$. The computational parame-

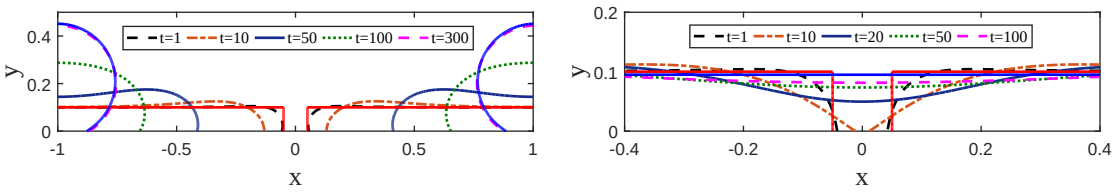

(a) $\theta_s=\frac{5\pi}{6}$ (b) $\theta_s=\frac{\pi}{6}$

Figure 7: (Example 4.6) The evolution of a thin film containing a hole in its center under different prescribed contact angles, where the red line and blue line represent the initial and numerical equilibrium states, respectively.

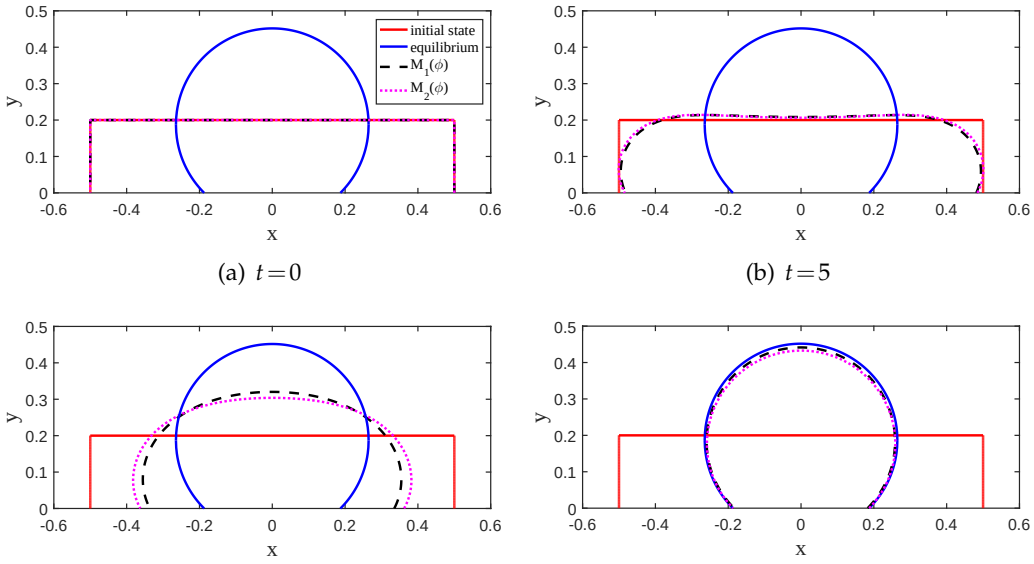

(a) $t=0$ (b) $t=5$

(c) $t=50$ (d) $t=300$

Figure 8: (Example 4.7) Numerical comparisons between the evolution with mobilities $M_1(\phi)=|1-\phi^2|+\varepsilon_M$ and $M_2(\phi)=(1-\phi^2)^2+\varepsilon_M$, where $\theta_s=\frac{3\pi}{4}$ and $\varepsilon=0.02$. The initial shape is a short island film, which is located in the region $[-0.5,0.5]\times[0,0.2]$. The blue lines represent the theoretical equilibrium shapes, which are constructed by the Winterbottom construction [28, 75].

ters are chosen as: the Young contact angle $\theta_s=\frac{3\pi}{4}$, the interface parameter $\varepsilon=0.02$, and the mesh size $\Delta x=\Delta y=0.002$.

The simulation in Fig. 8 shows how the film which corresponds to the mobility $M_1(\phi)$ evolves clearly faster than the film corresponding to $M_2(\phi)$. In particular, the film with $M_1(\phi)$ achieves its equilibrium at approximately $t=300$ (see Fig. 8(d)), whereas the film corresponding to $M_2(\phi)$ needs significantly longer. Furthermore, we observe that the evolution corresponding to the mobility $M_2(\phi)$ is not only slower, but also differs qualitatively in view of the valley which forms in the middle of the island film (see Fig. 8(c)).

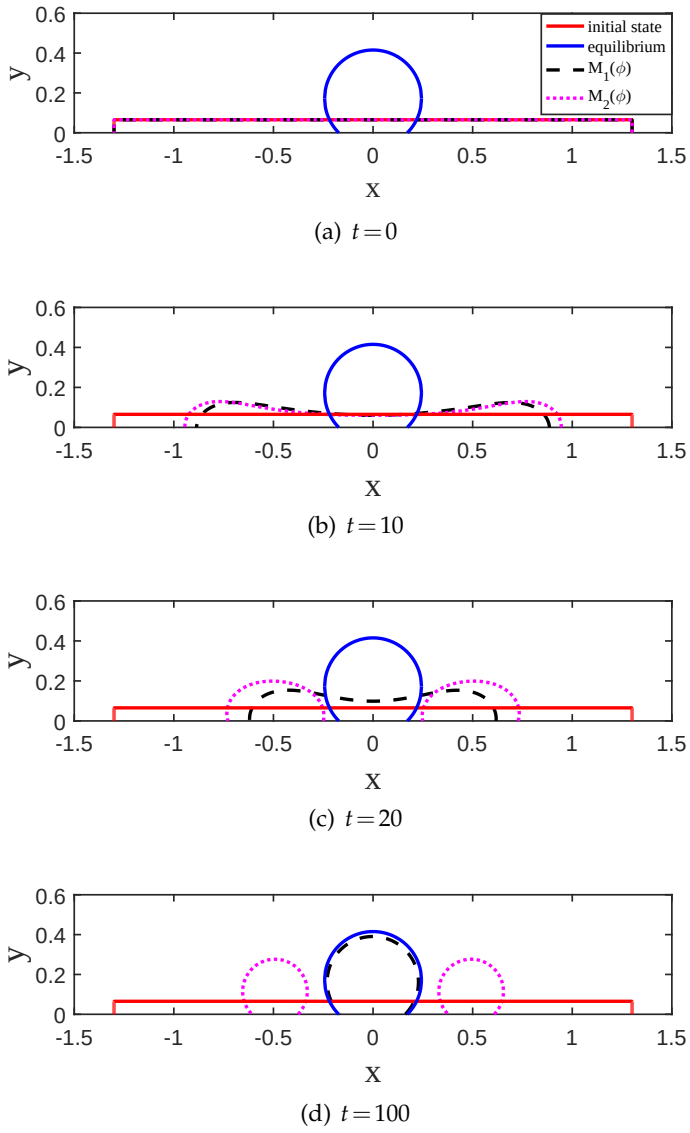

(a) $t=0$

(b) $t=10$

(c) $t=20$

(d) $t=100$

Figure 9: (Example 4.7) Numerical comparisons between the evolution with mobilities $M_1(\phi)=|1-\phi^2|+\varepsilon_M$ and $M_2(\phi)=(1-\phi^2)^2+\varepsilon_M$, where $\theta_s=\frac{3\pi}{4}$ and $\varepsilon=0.02$. The initial shape is a long island film, which is located in the region $[-1.3,1.3]\times[0,0.065]$.

These numerical results are consistent with the results reported in [35]. Furthermore, for an initially long island film, as shown in Fig. 9, we observe that the film which corresponds to the mobility $M_1(\phi)=|1-\phi^2|+\varepsilon_M$ does not pinch-off, and finally forms a circular equilibrium shape; while the film corresponding to $M_2(\phi)=(1-\phi^2)^2+\varepsilon_M$ pinches off into two separate pieces, and finally forms two isolated particles.

5 Conclusion

In this paper, we proposed an efficient, unconditionally energy-stable numerical scheme for solving the phase-field model about the kinetic evolution of solid-state dewetting of thin films. The phase-field model includes isotropic Cahn-Hilliard equation with degenerate mobility coupled with dynamic contact line boundary conditions. We then constructed two unconditionally energy-stable, efficient linear first-order IEQ/BDF1 and second-order IEQ/BDF2 numerical schemes to solve the phase-field model, and we proved that these numerical schemes satisfy the energy dissipation and mass conservation properties. Lots of numerical simulations were presented to demonstrate the accuracy and high efficiency of the proposed schemes. In addition, numerical simulations also investigated several interesting solid-state dewetting phenomena under different Young contact angles, and the influence of the contact line mobility η and different choices of degenerate mobilities $M(\phi)$ on the evolution process. In the future, we plan to include the surface energy anisotropy effect into the phase field model, and develop efficient numerical schemes to solve the anisotropic phase field model for investigating many of the complexities associated with solid-state dewetting experiments.

Acknowledgments

This work was partially supported by the National Natural Science Foundation of China Nos. 91630313, 11671312, 11871384 and Natural Science Foundation of Hubei Province No. 2018CFB466. The numerical calculations in this paper have been done on the supercomputing system in the Supercomputing Center of Wuhan University.

References

[1] E. Jiran, C. V. Thompson, Capillary instabilities in thin films, J. Electron. Mater. 19 (1990) 1153–1160.
[2] E. Jiran, C. V. Thompson, Capillary instabilities in thin continuous films, Thin Solid Films 208 (1992) 23–28.
[3] J. Ye, C. V. Thompson, Mechanisms of complex morphological evolution during solid-state dewetting of single-crystal nickel thin films, Appl. Phys. Lett. 97 (2010) 071904.
[4] J. Ye, C. V. Thompson, Regular pattern formation through the retraction and pinch-off of edges during solid-state dewetting of patterned single crystal films, Phys. Rev. B 82 (2010) 193408.
[5] J. Ye, C. V. Thompson, Anisotropic edge retraction and hole growth during solid-state dewetting of single-crystal nickel thin films, Acta Mater. 59 (2011) 582–589.
[6] J. Ye, C. V. Thompson, Templated solid-state dewetting to controllably produce complex patterns, Adv. Mater. 23 (2011) 1567–1571.
[7] C. V. Thompson, Solid-state dewetting of thin films, Annu. Rev. Mater. Res. 42 (2012) 399–434.

[8] F. Leroy, F. Cheynis, Y. Almadori, *et. al.*, How to control solid state dewetting: A short review, Surface Sci. Rep. 71 (2016) 391–409.
[9] D. T. Danielson, D. K. Sparacin, J. Michel, L. C. Kimerling, Surface-energy-driven dewetting theory of silicon-on-insulator agglomeration, J. Appl. Phys. 100 (2006) 083507.
[10] L. Armelao, D. Barreca, G. Bottaro, *et. al.*, Recent trends on nanocomposites based on Cu, Ag and Au clusters: A closer look, Coord. Chem. Rev. 250 (2006) 1294–1314.
[11] S. Rath, M. Heilig, H. Port, J. Wrachtrup, Periodic organic nanodot patterns for optical memory, Nano Lett. 7 (2007) 3845–3848.
[12] S. J. Randolph, J. D. Fowlkes, A. V. Melechko, *et. al.*, Controlling thin film structure for the dewetting of catalyst nanoparticle arrays for subsequent carbon nanofiber growth, Nanotechnology 18 (2007) 465354.
[13] V. Schmidt, J. V. Wittemann, S. Senz, U. Gosele, Silicon nanowires: A review on aspects of their growth and their electrical properties, Adv. Mater. 21 (2009) 2681–2702.
[14] H. Wong, P. W. Voorhees, M. J. Miksis, S. H. Davis, Periodic mass shedding of a retracting solid film step, Acta Mater. 48 (2000) 1719–1728.
[15] E. Dornel, J. C. Barbé, F. d. Crécy, *et. al.*, Surface diffusion dewetting of thin solid films: Numerical method and application to Si/SiO_2, Phys. Rev. B 73 (2006) 115427.
[16] W. Jiang, W. Bao, C. V. Thompson, D. J. Srolovitz, Phase field approach for simulating solid-state dewetting problems, Acta Mater. 60 (2012) 5578–5592.
[17] W. Jiang, Y. Wang, D. J. Srolovitz, W. Bao, Solid-state dewetting on curved subtrates, Phys. Rev. Mater. 2 (2018) 113401.
[18] W. Jiang, Q. Zhao, T. Qian, D. J. Srolovitz, W. Bao, Application of the Onsager's variational principle to the dynamics of a solid toroidal island on a substrate, Acta Mater. 163 (2019) 154–160.
[19] M. Naffouti, R. Backofen, M. Salvalaglio, *et. al.*, Complex dewetting scenarios of ultrathin silicon films for large-scale nanoarchitectures, Sci. Adv. 3 (2017) 1472.
[20] P. G. d. Gennes, Wetting: Statics and dynamics, Rev. Mod. Phys. 57 (1985) 827–863.
[21] W. Ren, W. E, Boundary conditions for the moving contact line problem, Phys. Fluids 19 (2) (2007) 022101.
[22] W. Ren, D. Hu, W. E, Continuum models for the contact line problem, Phys. Fluids 22 (2010) 102103.
[23] X. Xu, X. Wang, Analysis of wetting and contact angle hysteresis on chemically patterned surfaces, SIAM J. Appl. Math. 71 (2011) 1753–1779.
[24] O. Bäumchen, L. Marquant, R. Blossey, *et. al.*, Influence of slip on the Rayleigh-Plateau rim instability in dewetting viscous films, Phys. Rev. Lett. 113 (2014) 014501.
[25] R. V. Craster, O. K. Matar, Dynamics and stability of thin liquid films, Rev. Mod. Phys. 81 (2009) 1131–1198.
[26] Y. Wang, W. Jiang, W. Bao, D. J. Srolovitz, Sharp interface model for solid-state dewetting problems with weakly anisotropic surface energies, Phys. Rev. B 91 (2015) 045303.
[27] W. Jiang, Y. Wang, Q. Zhao, D. J. Srolovitz, W. Bao, Solid-state dewetting and island morphologies in strongly anisotropic materials, Scr. Mater. 115 (2016) 123–127.
[28] W. Bao, W. Jiang, D. J. Srolovitz, Y. Wang, Stable equilibria of anisotropic particles on substrates: A generalized Winterbottom construction, SIAM J. Appl. Math. 77 (2017) 2093–2118.
[29] W. Bao, W. Jiang, Y. Wang, Q. Zhao, A parametric finite element method for solid-state dewetting problems with anisotropic surface energies, J. Comput. Phys. 330 (2017) 380–400.
[30] W. Jiang, Q. Zhao, Sharp-interface approach for simulating solid-state dewetting in two dimensions: A Cahn-Hoffman ξ-vector formulation, Physica D 390 (2019) 69–83.

[31] D. J. Srolovitz, S. A. Safran, Capillary instabilities in thin films: I. energetics, J. Appl. Phys. 60 (1986) 247–254.
[32] M. Du, Pand Khenner, H. Wong, A tangent-plane marker-particle method for the computation of three-dimensional solid surfaces evolving by surface diffusion on a substrate, J. Comput. Phys. 229 (2010) 813–827.
[33] Q. Zhao, A sharp-interface model and its numerical approximation for solid-state dewetting with axisymmetric geometry, J. Comput. Appl. Math. 361 (2019) 144–156.
[34] W. Jiang, Q. Zhao, W. Bao, Sharp-interface approach for simulating solid-state dewetting in three dimensions, ArXiv:1902.05272.
[35] M. Dziwnik, A. Münch, B. Wagner, An anisotropic phase-field model for solid-state dewetting and its sharp-interface limit, Nonlinearity 30 (2017) 1465–1496.
[36] E. B. Dussan V., On the spreading of liquids on solid surfaces: static and dynamic contact lines, Annu. Rev. Fluid Mech. 11 (1) (1979) 371–400.
[37] T. Qian, X.-P. Wang, P. Sheng, Molecular scale contact line hydrodynamics of immiscible flows, Phys. Rev. E 68 (1) (2003) 016306.
[38] T. Qian, X.-P. Wang, P. Sheng, A variational approach to the moving contact line hydrodynamics, J. Fluid Mech. 564 (2006) 333–360.
[39] Q. He, R. Glowinski, X.-P. Wang, A least-squares/finite element method for the numerical solution of the Navier-Stokes-Cahn-Hilliard system modeling the motion of the contact line, J. Comput. Phys. 230 (12) (2011) 4991–5009.
[40] M. Gao, X.-P. Wang, A gradient stable scheme for a phase field model for the moving contact line problem, J. Comput. Phys. 231 (4) (2012) 1372–1386.
[41] M. Gao, X.-P. Wang, An efficient scheme for a phase field model for the moving contact line problem with variable density and viscosity, J. Comput. Phys. 272 (2014) 704–718.
[42] A. J. Salgado, A diffuse interface fractional time-stepping technique for incompressible two-phase flows with moving contact lines, ESAIM: M2AN 47 (3) (2013) 743–769.
[43] S. Aland, F. Chen, An efficient and energy stable scheme for a phase-field model for the moving contact line problem, Int. J. Numer. Methods Fluids 81 (11) (2016) 657–671.
[44] J. Shen, X. Yang, H. Yu, Efficient energy stable numerical schemes for a phase field moving contact line model, J. Comput. Phys. 284 (2015) 617–630.
[45] H. Yu, X. Yang, Numerical approximations for a phase-field moving contact line model with variable densities and viscosities, J. Comput. Phys. 334 (2017) 665–686.
[46] L. Ma, R. Chen, X. Yang, H. Zhang, Numerical approximations for Allen-Cahn type phase field model of two-phase incompressible fluids with moving contact lines, Commun. Comput. Phys. 21 (3) (2017) 867–889.
[47] L. Q. Chen, J. Shen, Applications of semi-implicit Fourier-spectral method to phase field equations, Comput. Phys. Commun. 108 (1998) 147–158.
[48] J. Zhu, L.-Q. Chen, J. Shen, V. Tikare, Coarsening kinetics from a variable-mobility Cahn-Hilliard equation: Application of a semi-implicit Fourier spectral method, Phys. Rev. E 60 (4) (1999) 3564–3572.
[49] D. Li, Z. Qiao, On second order semi-implicit Fourier spectral methods for 2D Cahn-Hilliard equations, J. Sci. Comput. 70 (1) (2017) 301–341.
[50] D. J. Eyre, Unconditionally gradient stable time marching the Cahn-Hilliard equation, MRS Proceedings 529 (1998) 39.
[51] A. Baskaran, J. S. Lowengrub, C. Wang, S. M. Wise, Convergence analysis of a second order convex splitting scheme for the modified phase field crystal equation, SIAM J. Numer. Anal. 51 (5) (2013) 2851–2873.

[52] D. Li, Z. Qiao, T. Tang, Characterizing the stabilization size for semi-implicit Fourier-spectral method to phase field equations, SIAM J. Numer. Anal. 54 (3) (2016) 1653–1681.
[53] J. Shen, X. Yang, Numerical approximations of Allen-Cahn and Cahn-Hilliard equations, Discrete Contin. Dyn. Syst 28 (4) (2010) 1669–1691.
[54] Q. Du, L. Ju, X. Li, Z. Qiao, Stabilized linear semi-implicit schemes for the nonlocal Cahn–Hilliard equation, J. Comput. Phys. 363 (2018) 39–54.
[55] F. Guillén-González, G. Tierra, On linear schemes for a Cahn-Hilliard diffuse interface model, J. Comput. Phys. 234 (2013) 140–171.
[56] X. Yang, Linear, first and second-order, unconditionally energy stable numerical schemes for the phase field model of homopolymer blends, J. Comput. Phys. 327 (2016) 294–316.
[57] X. Yang, J. Zhao, Q. Wang, J. Shen, Numerical approximations for a three components Cahn-Hilliard phase-field model based on the invariant energy quadratization method, Math. Models Methods Appl. Sci. 27 (11) (2017) 1993–2030.
[58] J. Zhao, X. Yang, Y. Gong, Q. Wang, A novel linear second order unconditionally energy stable scheme for a hydrodynamic Q-tensor model of liquid crystals, Comput. Methods Appl. Mech. Eng. 318 (2017) 803–825.
[59] J. Zhao, Q. Wang, X. Yang, Numerical approximations for a phase field dendritic crystal growth model based on the invariant energy quadratization approach, Int. J. Numer. Meth. Engng. 110 (3) (2017) 279–300.
[60] R. Chen, X. Yang, H. Zhang, Second order, linear and unconditionally energy stable schemes for a hydrodynamic model of smectic-A liquid crystals, SIAM J. Sci. Comput. 39 (6) (2017) A2808–A2833.
[61] X. Yang, Numerical approximations for the Cahn-Hilliard phase field model of the binary fluid-surfactant system, J. Sci. Comput. 74 (2018) 1533–1553.
[62] X. Yang, H. Yu, Efficient second order unconditionally stable schemes for a phase field moving contact line model using an invariant energy quadratization approach, SIAM J. Sci. Comput. 40 (3) (2018) B889–B914.
[63] J. Shen, J. Xu, J. Yang, A new class of efficient and robust energy stable scheme for gradient flows, SIAM Rev. (2017) to appear.
[64] J. Shen, J. Xu, J. Yang, The scalar auxiliary variable (SAV) approach for gradient flows, J. Comput. Phys. 353 (2018) 407–416.
[65] Q. Cheng, J. Shen, X. Yang, Highly efficient and accurate numerical schemes for the epitaxial thin film growth models by using the SAV approach, J. Sci. Comput. 78 (2019) 1467–1487.
[66] Q. Cheng, J. Shen, Multiple scalar auxiliary variable (MSAV) approach and its application to the phase-field vesicle membrane model, SIAM J. Sci. Comput. 40 (6) (2018) A3982–A4006.
[67] C. Chen, X. Yang, Fast, provably unconditionally energy stable, and second-order accurate algorithms for the anisotropic Cahn-Hilliard model, Comput. Meth. Appl. Mech. Engrg. 351 (2019) 35–59.
[68] X. Yang, D. Han, Linearly first- and second-order, unconditionally energy stable schemes for the phase field crystal model, J. Comput. Phys. 330 (2017) 1116–1134.
[69] L. Modica, S. Mortola, Il limite nella Γ-convergenza di una famiglia di funzionali ellittici, Boll. Un. Mat. Ital. A 14 (3) (1977) 526–529.
[70] Q. Zhao, W. Jiang, D. J. Srolovitz, W. Bao, Triple junction drag effects during topological changes in the evolution of polycrystalline microstructures, Acta Mater. 128 (2017) 345–350.
[71] J. W. Cahn, C. M. Elliott, A. Novickcohen, The Cahn-Hilliard equation with a concentration dependent mobility: motion by minus the Laplacian of the mean curvature, European J. Appl. Math. 7 (03) (1996) 287–301.

[72] S. Dai, Q. Du, Weak solutions for the Cahn-Hilliard equation with degenerate mobility, Arch. Rational. Mech. Anal. 219 (3) (2016) 1161–1184.
[73] A. A. Lee, A. Muznch, E. Suzli, Sharp-interface limits of the Cahn–Hilliard equation with degenerate mobility, SIAM J. Appl. Math. 76 (2) (2016) 433–456.
[74] X. Yang, J. Zhao, X. He, Linear, second order and unconditionally energy stable schemes for the viscous Cahn-Hilliard equation with hyperbolic relaxation using the invariant energy quadratization method, J. Comput. Appl. Math. 343 (2018) 80–97.
[75] W. L. Winterbottom, Equilibrium shape of a small particle in contact with a foreign substrate, Acta Metall. 15 (2) (1967) 303–310.
[76] U. Czubayko, V. G. Sursaeva, G. Gottstein, L. S. Shvindlerman, Influence of triple junctions on grain boundary motion, Acta Mater. 46 (16) (1998) 5863–5871.
[77] M. Upmanyu, D. J. Srolovitz, L. S. Shvindlerman, G. Gottstein, Molecular dynamics simulation of triple junction migration, Acta Mater. 50 (6) (2002) 1405–1420.
[78] D. J. Srolovitz, S. A. Safran, Capillary instabilities in thin films: II. kinetics, J. Appl. Phys. 60 (1986) 255–260.